Comparing the Damping Capabilities of different Fast-Frequency Controlled Demand Technologies

Johanna Vorwerk*, Uros Markovic, Gabriela Hug
Power Systems Laboratory, ETH Zurich, Zurich, Switzerland
*vorwerk@eeh.ee.ethz.ch

***Abstract*—Modern power systems require an additional supply of fast-frequency reserves to cope with the reduction in overall system inertia and damping caused by the increasing share of inverter-interfaced generation. Batteries are commonly referred to as the most promising option to provide such reserves due to their fast activation capabilities. In this work, we show that inverter-interfaced thermal loads, i.e. heat pumps and refrigeration, tend to accommodate a slightly quicker response than batteries and can thus compete with their dynamic characteristics. To this end, we derive characteristic single-input single-output transfer functions that describe the linearized response of different technologies and include detailed load characteristics. The performed time-domain studies for a low-inertia scenario clearly show that thermal loads can improve frequency damping to the same extent as batteries.**

***Index Terms*—Fast-frequency reserve, low-inertia systems, demand side resources, variable speed drives, batteries**

I. Introduction

The increasing share of converter-interfaced generation in power systems imposes challenges on the operation of such low-inertia systems. One of them is the presence of fast and often underdamped frequency dynamics that increase the need for rapid frequency regulation [1]. Even though various generation and load technologies have been proposed for providing fast-frequency reserve, batteries are commonly thought of as the most promising candidate [2].

As variable speed drive (VSD) technology is emerging in thermal loads such as heat pumps, refrigerators and air conditioners, recent literature suggests benefits from their continuously controllable operation range. Several studies propose different control options for frequency support from induction machine based thermal or industrial loads. In particular, [3] estimates the potential for reserve provision with industrial induction machines in Great Britain, whereas [4] proposes a control scheme for VSD air conditioning. Furthermore, [5] extends the approach in [3] and uses an adaptive strategy to avoid regeneration of the motor while supplying frequency droop control. Recently, [6] developed an inertia emulation scheme for general smart induction motor variable frequency drives, while [7] suggested a virtual inertia control scheme specifically for heat pumps. The latter includes a small-signal model for heat pumps and a detailed representation of load side characteristics. Similar modeling for VSD-based refrigeration driven by a brushless DC motor (BLDC) has been proposed in [8]. While most of these papers exploit the improvements achieved through their control algorithms and study underlying stability regions, none of them assess potential restrictions from the thermal dynamics or compare the obtained frequency response to other fast-frequency reserve supply technologies such as batteries.

In addition, the damping contribution from demand-side resources has received little attention in current literature. Even though the work in [9] was motivated by the increasing share of controllable loads in smart grids, it focuses on the impact of the load-damping coefficient in linear frequency studies without modeling the loads as such. Nonetheless, this work emphasizes the importance of accurate inclusion of load damping contribution for frequency stability. The studies performed in [10] included a more detailed load model, but the applied demand response scheme is limited to load shedding. It does neither incorporate technology-specific models nor continuously controllable methods.

This paper tackles the topic by assessing whether the frequency reserve supplied by VSD thermal loads is compatible with the one offered by batteries. The contributions of our work are threefold:

- We formulate simple Single Input Single Output (SISO) transfer function models for thermal demand response technologies and battery systems suitable for small-signal frequency stability studies in low-inertia power systems. Since VSD heat pumps (VSD-HP) and VSD refrigeration (VSDR) employ different motor types, these two have been selected as representatives for thermal loads.
- We showcase and compare the practicality of thermal demand response technologies in damping frequency oscillations in inverter-dominated systems.
- We compare the fast-frequency response contribution of VSD-HP and VSDR technology to batteries.

The remainder of the paper is structured as follows: In Section II, we present the system modeling encompassing the derivation of SISO transfer functions for VSDR, VSD-HP and battery (BESS) unit. Section IV demonstrates the time-domain performance of the different reserve options on several case studies, whereas Section V concludes the paper.

II. System Modeling

The demand response technologies considered in this paper include variable speed thermal devices, i.e. a refrigerator and a heat pump, as well as a battery (BESS). An overview of the implemented system for linear frequency response studies is shown in Fig. 1. The respective colors and transfer functions indicate the contribution of the considered demand response technologies.

The considered grid equivalent exhibits fast frequency dynamics and accounts for traditional primary frequency reserve

978-1-6654-3597-0/21/$31.00

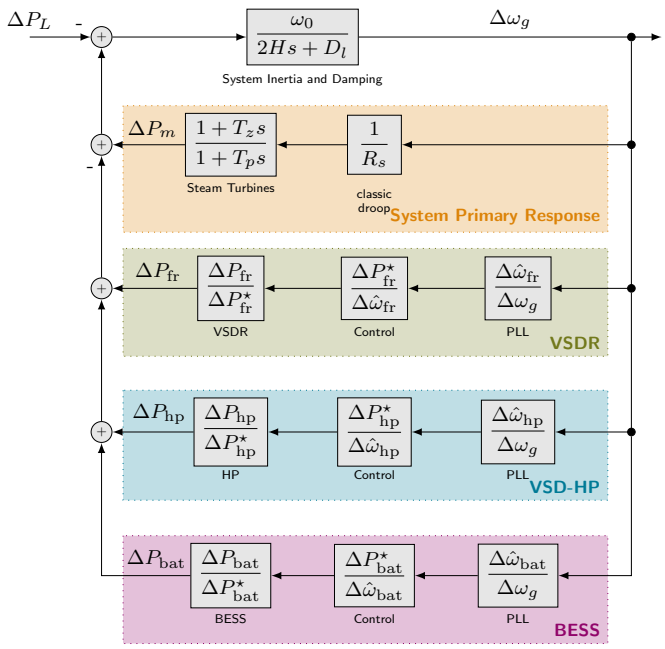

Fig. 1. Block diagram of the linearized small-signal test system.

provision simultaneously. The primary response block diagram in Fig. 1 was previously proposed in [11] and provides a suitable grid equivalent for summarizing the effects of inertial response and primary frequency control of an external system with simple transfer functions. As a result, the frequency dynamics can be adjusted and controlled by tuning the time constants (T_z, T_p), the system inertia H and the primary frequency droop constant R_s.

In addition, Fig. 1 suggests that the contribution of the demand response technologies can be split into three separate components as:

$$\frac{\Delta P_x}{\Delta\omega_g} = \underbrace{\frac{\Delta\hat{\omega}_x}{\Delta\omega_g}}_{\text{PLL specific}} \cdot \underbrace{\frac{\Delta P^{\star}_x}{\Delta\hat{\omega}_x}}_{\text{Control specific}} \cdot \underbrace{\frac{\Delta P_x}{\Delta P^{\star}_x}}_{\text{Device specific}}, \tag{1}$$

where $\Delta\hat{\omega}_x$ is the estimation of the grid frequency $\Delta\omega_g$, $\Delta P^{\star}_x$ is the active power reference and ΔP_x is the actual terminal power of the technology x.

As this study aims to assess the differences in internal dynamic performance imposed by the load characteristics of the technologies themselves, all devices have the same synchronization and frequency control schemes. Thus, the first two contributions to each technology's overall transfer function will be exactly the same. The remainder of this section will first detail the synchronization unit and control scheme modeling before considering each technology separately.

A. Synchronization Unit

For grid synchronization, standard synchronous reference frame phase-locked loops (SRF-PLL) are employed. This configuration is currently one of the simplest and most commonly used for various converter interfaced applications [12]. Even though low-power refrigeration is connected via a single phase to the grid, the resulting difference in the phase-detection scheme is omitted in the presented work to focus on the load-side dynamics. In particular, the phase detectors within the PLLs are assumed to operate ideal, independent of the actual method installed. The frequency for each of the three technologies is estimated as presented in [13]. The transfer function G_{Pll} is characterized by the proportional and integral controller gains $k_{p,pll}, k_{i,pll}$ and the base frequency ω_b. The estimated frequency $\Delta\hat{\omega}_x$ tracks the grid frequency $\Delta\omega_g$ as follows:

$$G_{\mathrm{Pll}} = \frac{\Delta\hat{\omega}_x}{\Delta\omega_g} = \frac{\omega_b(k_{p,pll}s + k_{i,pll})}{s^2 + \omega_b k_{p,pll}s + \omega_b k_{i,pll}}. \tag{2}$$

B. Frequency Control Scheme

Due to the focus on comparing the inherent dynamic behavior of different demand response technologies rather than assessing control strategies, the same standard frequency droop controller is employed for all three investigated technologies. Therefore, the required change of active power $\Delta P^{\star}_x$ for a technology x is proportional to the estimated frequency deviation $\Delta\hat{\omega}_x$, described by the transfer function of the form

$$\Delta P^{\star}_x = d_f \Delta\hat{\omega}_x, \tag{3}$$

with d_f being the frequency droop gain.

III. Demand Response Technologies

This section presents the transfer function models for each of the studied demand response devices. While the heat pump model is taken from [7], the battery and VSDR models are obtained by simplifying the set of differential algebraic equations (DAEs) presented in [14] and our previous work in [8], respectively[1]. Nonetheless, the modeling of each technology requires certain assumptions. Besides considering the small-signal model to be valid, it is assumed that no limits of the converter interface and system components are reached, which is reasonable for adequate frequency droop control gains. In particular, neither will the thermal loads be switched off during operation nor will the battery shift into discontinuous conduction mode.

A. Variable Speed Refrigeration

The considered refrigeration unit is based on a brushless DC motor (BLDC) that allows for variable speed operation of the compressor. The latter extracts the heat from a refrigeration chamber. The motor is connected to the grid via two back-to-back converters that permit the control of the BLDC's rotational speed, thus allowing continuous manipulation of the active power consumption. To formulate a SISO-transfer function, the non-linear model presented in [8] and depicted in Fig. 2 is simplified and linearized. Since the goal is to find a transfer function capturing the active power change following a frequency disturbance, several assumptions were made: (i) The active power change at the terminal p_t is solely determined by the power change following a change in the rotational speed of the motor ω_m in the refrigeration unit. Therefore, the DC-link dynamics are negligible. (ii) The rectifier controls, i.e. the DC-voltage v_{dc} and terminal current

[1]Note that, to enhance the readability of the notation, identical symbols will be used to denote some of the quantities within the individual technologies, e.g. the symbol H will refer to the motor and compressor inertia constant of that particular device. Besides, linearized variables are labeled with Δ.

i_t control, have a fast tracking performance that does not significantly influence the overall change in active power. Thus, they are negligible and the power factor at the terminal is unity. (iii) The rectifier and inverter operate losslessly. Thus the power at the AC terminals equals the DC link power and the BLDC motor power. (iv) The temperature control dynamics are significantly slower than those associated with the supply of fast-frequency reserve. Moreover, the activation time will not affect the refrigeration compartment's temperature T_f significantly. Thus it is neglected. Nonetheless, the temperature dynamics govern the initial quasi-steady-state operation point. As a result, the final VSDR model includes the active power and inverter controllers, the BLDC and the compressor dynamics, as indicated by the green box in Fig. 2. Note that the inverter controls consist of cascaded rotational speed and motor current loops. Furthermore, the equality $p_t = P_{\text{fr}} = P_{\text{dc}}$ holds.

The active power control loop processes the active power reference $\Delta P^{\star}_{\text{fr}}$ from the frequency droop controller, compares it to the measured terminal power ΔP_{lpf} and computes the required change in BLDC's rotational speed $\Delta\omega^{\star}_m$ as

$$\Delta\omega^{\star}_m = \left(k_{pp} + k_{ip}s^{-1}\right)\left(\Delta P^{\star}_{\text{fr}} - \Delta P_{\text{lpf}}\right), \tag{4}$$

where k_{pp} and k_{ip} are the proportional and integral active power control gains. Subsequently, the speed setpoint is passed to the cascaded speed and current PI-control loops of the inverter controls that output the required BLDC motor voltage $v^{\star}_m$. Assuming good tracking performance of the inner current control loop, the motor current can be formulated as:

$$\Delta i_m = \frac{k_{p\omega}s + k_{i\omega}}{s(\tau_c s + 1)}\left(\Delta\omega^{\star}_m - \Delta\omega_m\right), \tag{5}$$

with $k_{p\omega}$ and $k_{i\omega}$ being the proportional and integral speed control gains, respectively, and τ_c denoting the time constant of the current control loop.

The BLDC voltage equation relates the line voltage Δv_m to the motor current and rotational speed via

$$\Delta v_m = \left(\frac{\ell_a}{\omega_b}s + r_a\right)\Delta i_m + k_e\Delta\omega_m, \tag{6}$$

where (ℓ_a, r_a) are the motor armature inductance and resistance and k_e is the motor back electromagnetic force constant. Furthermore, the motor swing equation relates the change in motor current Δi_m and compressor load torque $\Delta\Gamma_c$ to the motor speed:

$$\Delta\omega_m = \frac{k_t\Delta i_m - \Delta\Gamma_c}{2Hs + b} = \frac{k_t}{2Hs + b + \frac{\Delta\Gamma_c}{\Delta\omega_m}}\Delta i_m, \tag{7}$$

with k_t being the motor torque constant, H the motor and compressor inertia and b the friction coefficient.

Assuming lossless conversion in the inverter unit and using the voltage equation in (6) as well as the swing equation in (7), the DC-link and thus refrigerator power $P_{\text{fr}} = v_m i_m$ are expressed as a linear function of the motor current:

$$\frac{\Delta P_{\text{fr}}}{\Delta i_m} = v_{m0} + i_{m0}\left(\frac{\ell_a}{\omega_b}s + r_a\right) + \frac{i_{m0}k_e k_t}{2Hs + b + \frac{\Delta\Gamma_c}{\Delta\omega_m}}. \tag{8}$$

The load torque in (8) is related to the rotational speed of the motor by $\Gamma_c = \omega_m p_c$, where p_c is the power consumed by the compressor. In [8], the compressor power was observed to follow a first-order transfer function

$$p_c = \frac{a_2\omega_m^2 + a_1\omega_m + a_0}{\tau_p s + 1}. \tag{9}$$

The coefficients a_i and time delay τ_p can be estimated from data sheets provided by manufacturers and were obtained in [8]. Linearizing and combining the torque and power expressions yields the transfer function of the compressor as:

$$\frac{\Delta\Gamma_c}{\Delta\omega_m} = p_{c0} + \frac{2a_2\omega_{m0} + a_1}{\tau_p s + 1}. \tag{10}$$

Finally, the DC-link power is measured and fed back to the power controller. The low-pass filtered power ΔP_{lpf} is obtained as:

$$\Delta P_{\text{lpf}} = \left(\tau_{\text{lpf}}s + 1\right)^{-1}\Delta P_{\text{fr}}. \tag{11}$$

From (4)-(11), the transfer function of the VSDR shown in Fig. 3 can be completed.

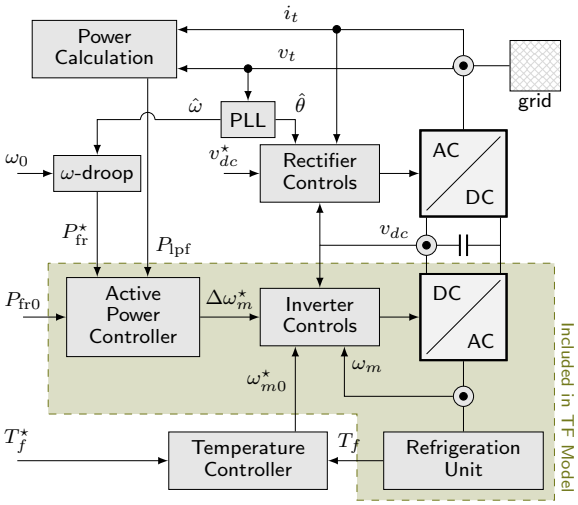

Fig. 2. Overview of the variable speed refrigeration control scheme.

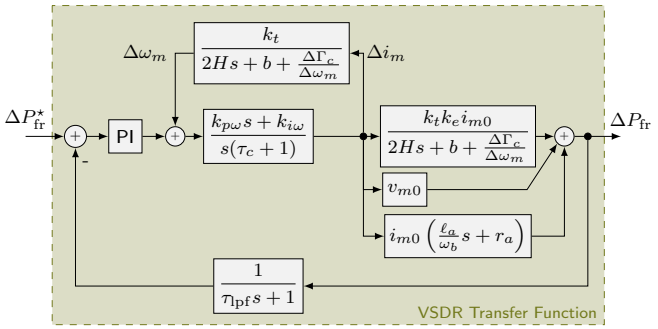

Fig. 3. Block diagram of the variable speed refrigerator transfer function.

B. Variable Speed Heat Pump

In general, a VSD-HP operates similar to the VSDR as displayed in Fig. 4, with the major differences to a refrigerator marked in blue. In particular, HPs employ induction motors (IMs). Thus, the VSD no longer controls the motor and compressor's speed (C) directly but manipulates the torque by employing a standard vector control technique. A complete transfer function model for a VSD-HP to supply inertia control was published in [7] and is described below.

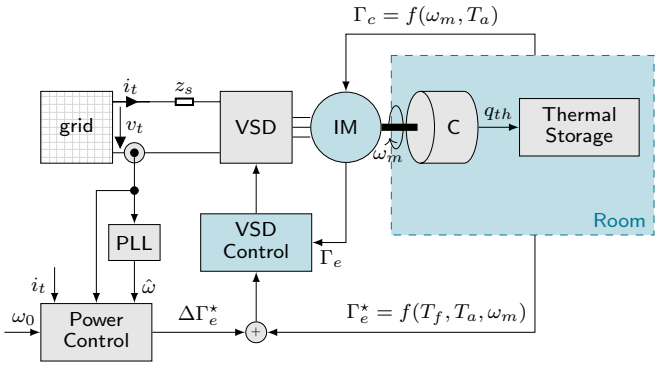

Fig. 4. Overview of the variable speed heat pump control scheme.

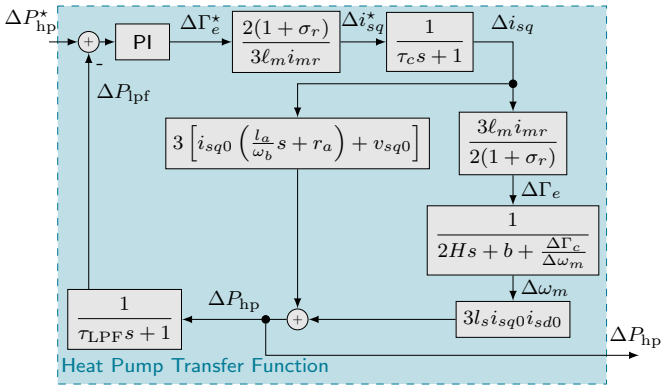

Fig. 5. Block diagram of the variable speed heat pump transfer function.

In accordance with the assumptions made for the refrigerating system, the following applies for the heat pump: (i) The thermal room dynamics are significantly slower than the grid dynamics of interest and thus can be neglected. Nonetheless, they determine the initial operating conditions. (ii) Both the inverter and rectifier are lossless and the rectifier controls ensure a power factor of unity. Thus the active terminal power equals the active power drawn from the motor.

As a result, the transfer function for the heat pump displayed in Fig. 5 is obtained. In particular, the IM is controlled by a sequence of power and internal vector torque control. The former compares the required active power deviation $\Delta P_{\text{hp}}^\star$ established by the frequency control scheme to the measured terminal power ΔP_{lpf} computed as in (11), and provides the electric torque reference $\Delta\Gamma_e^\star$ by employing proportional-integral control with the gains k_{pp} and k_{ip}:

$$\Delta\Gamma_e^\star = \left(k_{pp} + k_{ip} s^{-1}\right)\left(\Delta P_{\text{hp}}^\star - \Delta P_{\text{lpf}}\right). \tag{12}$$

The inner control first transforms the torque setpoint into a current reference by synchronizing a rotational reference frame with the rotor field of the IM. As a result, the stator current reference $\Delta i_{sq}^\star$ is proportional to the reference torque. Assuming good tracking of the subsequent q-axis current control, the stator q-axis current Δi_{sq} is given by

$$\Delta i_{sq} = \underbrace{\frac{1}{\tau_c s+1}}_{i_{sq}\text{-control}} \cdot \underbrace{\frac{2\left(1+\sigma_r\right)}{3\ell_m i_{mr}}}_{\text{reference transformation}} \Delta\Gamma_e^\star, \tag{13}$$

where τ_c is the delay of the PI-current control, ℓ_m and i_{mr} are the magnetizing inductance and current, respectively, and $\sigma = \frac{\ell_r}{\ell_m}$, with ℓ_r denoting the rotor inductance.

The motor electric torque $\Delta\Gamma_e$ follows from the IM dynamics and can be expressed in terms of the stator current by applying the back-transformation:

$$\Delta\Gamma_e = \frac{3\ell_m i_{mr}}{2(\sigma_r+1)} \Delta i_{sq}. \tag{14}$$

The effect of the electric and compressor torque on the speed of the IM are determined by a swing equation

$$\Delta\omega_m = \left(2Hs + b + \frac{\Delta\Gamma_c}{\Delta\omega_m}\right)^{-1} \Delta\Gamma_e. \tag{15}$$

Due to the lossless operation of the VSD and the motor q-axis voltage equation, the active power is formulated as:

$$\Delta P_{\text{hp}} = 3\Delta i_{sq}\left[i_{sq0}\left(\frac{\ell_a}{\omega_b}s + r_a\right) + v_{sq0}\right] + 3\ell_s i_{sq0} i_{sd0} \Delta\omega_m, \tag{16}$$

where $\ell_a = \ell_s - \frac{\ell_m^2}{\ell_r}$ and $r_a = r_s + \frac{r_s \ell_s}{\ell_r}$ are machine constants, and (r_s, l_s) denote the stator parameters.

Similar to the refrigerator, the dynamic heat pump and compressor models are formulated in terms of a transfer function [15]. Following a change in rotational speed $\Delta\omega_m$, the torque change $\Delta\Gamma_c$ is described by

$$\Delta\Gamma_c = \left(\frac{n_{\omega 1} s + n_{\omega 0}}{s^2 + d_{\omega 1} s + d_{\omega 0}} - \Gamma_{c0}\right) {\omega_{m0}}^{-1} \Delta\omega_m, \tag{17}$$

where the parameters d_ω and n_ω are obtained from [15] by using a polynomial regression algorithm. This step completes the VSD-HP transfer function depicted in Fig. 5.

C. Battery

The battery model is based on the DAE model presented in [14]. In general, the control scheme shown in Fig. 6 significantly deviates from the one for the thermal loads, since the load is only indirectly activated. The battery connects to the grid with a sequence of a rectifier and a buck-boost converter. While the control objectives for the first stage are to control the terminal power $(p^\star, q^\star)$, frequency ω_c and voltage v_c, as is common for voltage source converters (VSCs), the control of the second stage ensures a stable DC-link voltage v_{dc}. Thus, if the terminal power reference changes, the rectifier controls will increase the current drawn from the DC-link i_{out} and the DC-link voltage will drop, causing the DC-DC-converter controls to draw more current i_b from the battery. As a result, the transfer function is split into an AC-side and a DC-side contribution:

$$\frac{\Delta P_{\text{bat}}}{\Delta P_{\text{bat}}^\star} = \frac{\Delta i_{\text{out}}}{\Delta P_{\text{bat}}^\star} \cdot \frac{\Delta P_{\text{bat}}}{\Delta i_{\text{out}}}. \tag{18}$$

The AC-side relates the required terminal power change $\Delta P_{\text{bat}}^\star$ to the required DC-current Δi_{out}, whereas the DC-side contribution includes the battery and DC-link dynamics to obtain the power change ΔP_{bat}. For our formulation to be valid, the following assumptions apply: (i) The change in active terminal power is determined by the power drawn

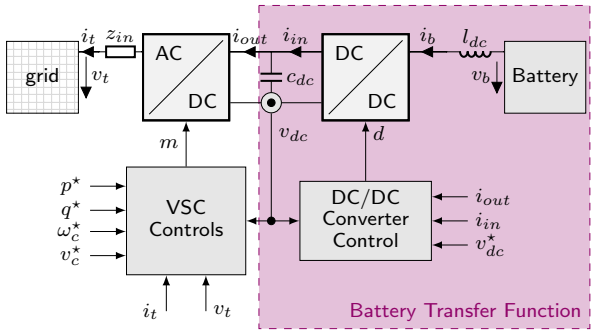

Fig. 6. Overview of the battery control scheme.

from the battery. (ii) The VSC inner control loops have good tracking performance. (iii) The conditions presented in [14] hold so that a zero-order model can capture the internal battery processes. (iv) The DC/DC-converter operates in continuous conduction and discharging mode.

As a result, the battery transfer function of the DC-side model includes all of the components indicated in purple in Fig. 6, and is described by the following algebraic and differential equations in (19) and (20), respectively:

$$v_b = v_{oc} - r_b i_b \tag{19a}$$
$$v_{\mathrm{dc}} i_{in} = v_b i_b \tag{19b}$$
$$i_{\mathrm{dc}}^\star = k_{pv}(v_{\mathrm{dc}}^\star - v_{\mathrm{dc}}) + k_{iv}\mu_v \tag{19c}$$
$$d = k_{pc}(i_{\mathrm{dc}}^\star + i_{\mathrm{out}} - i_{in}) + k_{ic}\mu_i \tag{19d}$$
$$P_{\mathrm{bat}} = v_{\mathrm{dc}} i_{\mathrm{out}} \tag{19e}$$

$$\dot{i}_b = \frac{\omega_b}{\ell_{\mathrm{dc}}}\left(v_b - (1-d)v_{\mathrm{dc}}\right) \tag{20a}$$
$$\dot{v}_{\mathrm{dc}} = \frac{\omega_b}{c_{\mathrm{dc}}}\left(i_{in} - i_{\mathrm{out}}\right) \tag{20b}$$
$$\dot{\mu}_v = v_{\mathrm{dc}}^\star - v_{\mathrm{dc}} \tag{20c}$$
$$\dot{\mu}_i = i_{\mathrm{dc}}^\star + i_{\mathrm{out}} - i_{in}. \tag{20d}$$

For a detailed description of the modeling process and parameter declaration, we refer the reader to [14].

A SISO transfer function with the desired input and output variables $G_{\mathrm{DC-bat}}$ can be derived by linearizing and transforming the DAE model into its state-space representation and from this derive the transfer function as follows:

$$\dot{x} = Ax + Bu, \quad y = Cx + Du, \tag{21}$$
$$G_{\mathrm{DC-bat}} = \frac{\Delta P_{\mathrm{bat}}}{\Delta i_{\mathrm{out}}} = C(sI - A)^{-1}B + D. \tag{22}$$

To obtain a transfer function with the desired input and output parameters, the input u is the DC current drawn from the rectifier i_{out} and the output y is the battery power P_{bat}, while the state vector x includes the battery current i_b, DC-link voltage v_{dc}, and the voltage and current integrator states μ_v, μ_c.

The current drawn from the AC side can be formulated as

$$i_{\mathrm{out}} = \underbrace{\frac{\Delta P_{bat}^\star}{v_{dc}^\star}}_{\text{compute } i_{\mathrm{out}}} \underbrace{\frac{1}{\tau_c s + 1}}_{\text{VSC control}}, \tag{23}$$

where τ_c is the time constant of the slowest and outermost inner control loop of the VSC. Combining (22) and (23) finalizes the formulation of the BESS transfer function.

IV. Time-Domain Case Studies

This section examines the system response for different configurations of fast-frequency support from the introduced demand response technologies. The system configurations considered in the case studies are defined in Table I. The chosen refrigeration capacity of 3 % is comparable to the actual share of residential cooling loads in electricity consumption of Switzerland [16], [17]. Note that achieving the same power contribution from different technologies requires different aggregation sizes, i.e. considering the nominal power displayed in Table II, 60 000 VSDR units, 3000 VSD-HPs and 30 battery systems are required in total.

For each case study, the system is subjected to a step decrease in system load power of $\Delta P_l = -0.1$ p.u. at time instance of $t = 0$ s. Some of the system parameters are defined in Table II, while all remaining technology-specific parameters and the initial operating conditions were taken from the corresponding literature in [7], [8], [14].

The results displayed in Fig. 7 indicate that the system is slightly underdamped for the base case scenario and exhibits a frequency nadir of 1.05 Hz. By adding any of the fast reserve response options, the frequency damping is significantly increased independent of the activated technology. More specifically, each of the three technologies is capable of reducing the frequency nadir by 0.2 Hz and thus enhancing the primary frequency reserves during transients. Nonetheless, the rate-of-change-of-frequency (RocoF) remains constant as well as the response time and steady-state frequency deviation.

Fig. 8 compares the different technologies during the transient response phase. Even though the performance is similar for all technologies, thermal loads tend to outperform the

TABLE I
Overview of performed case studies.

Case Study Identifier	**Capacity of Demand Technology** in % of system load		
	VSDR	**VSD-HP**	**BESS**
1	0	0	0
2-FR	3 %	0	0
2-HP	0	3 %	0
2-Bat	0	0	3 %

TABLE II
System parameters. All other parameters where taken from [7], [8], [14] and transformed to the per unit system.

Grid Equivalent		**Pll**	
H	0.5 s	$k_{p,pll}$	0.4 p.u.
R_d	0.02 p.u.	$k_{i,pll}$	4.69 p.u. s^{-1}
D_l	0.2 p.u.	**Frequency Droop**	
T_z	0.5 s	d_f	50 p.u.
T_p	9 s	**Nominal Power**	
base power	200 MW	VSDR	0.1 kW
base frequency	50 Hz	VSD-HP	2 kW
		BESS	200 kW

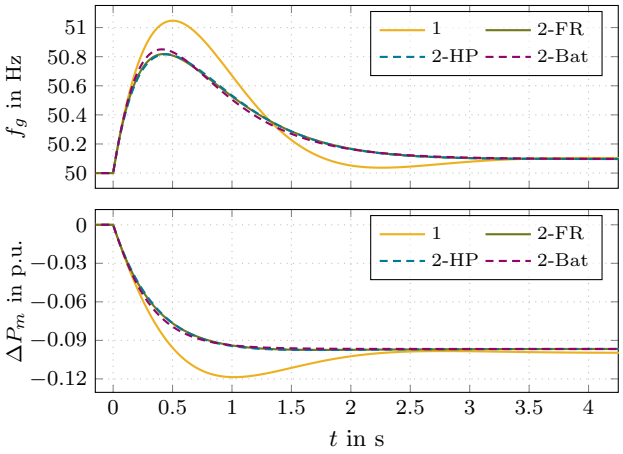

Fig. 7. Overview of the load power, grid frequency and mechanical power after a disturbance in load power for all the test cases.

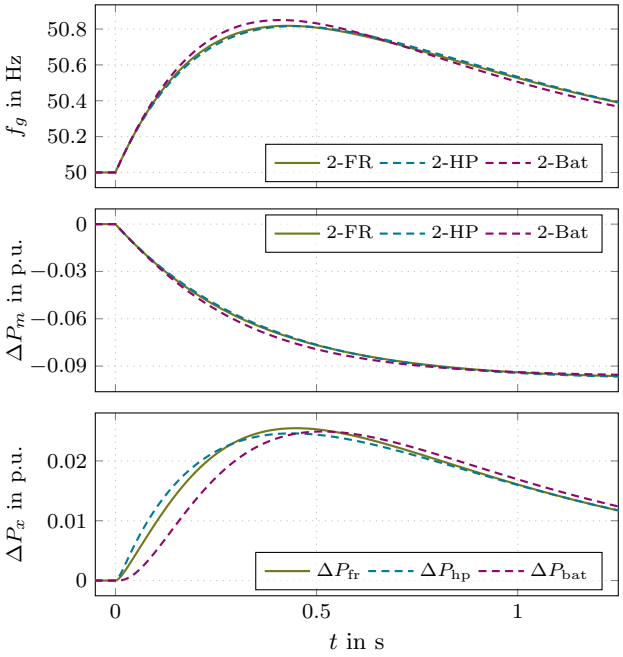

Fig. 8. Results for the second test case: grid frequency, mechanical power and terminal power of the individual technologies.

batteries slightly and are undeniably capable of supplying a competitive response. Moreover, thermal loads show faster activation and result in a lower frequency nadir.

In conclusion, the two thermal loads, more precisely VSDR and VSD-HP, show little deviation in their response despite the different motor types and internal control loops. Both load models slightly outperform the reserve supplied by batteries for the selected operation point, and hence are justified alternatives for the supply of fast-frequency support. However, the effect of the converter and motor limits, as well as the initial operating condition on the effectiveness of the reserve remains to be studied.

V. Conclusion

This paper compares the fast-frequency response provided by VSD thermal loads to the one offered by batteries. Therefore, SISO transfer function models that include detailed load dynamics were developed for each of the technologies. The conducted case study not only confirms current literature on the practicality of VSD-based thermal loads for fast-frequency reserves but also suggests that even with proportional control a small fraction of system load has a significant potential to enhance frequency damping.

The thermal loads under investigation showcased similar frequency responses. In particular, the frequency nadir was significantly reduced while RoCoF and steady-state frequency deviation were not affected. Comparing the thermal loads to batteries, the former accomplish a higher reduction of frequency nadir, while batteries show a delayed response.

The converter, motor and battery limits remain to be added for a follow-up study. Besides, the availability of the resources, e.g. the seasonality in heat pumps, should be included when discussing the technologies' usability in a larger scope. Nonetheless, the results based on linear modeling already indicate that thermal loads are as capable as batteries for supplying fast-frequency reserve.

References

[1] F. Milano, F. Dörfler, G. Hug, D. J. Hill, and G. Verbič, "Foundations and challenges of low-inertia systems," in *PSCC*, Dublin, 2018, pp. 1–25.

[2] H. Karbouj, Z. H. Rather, D. Flynn, and H. W. Qazi, "Non-synchronous fast frequency reserves in renewable energy integrated power systems: A critical review," *Int. J. Electr. Power Energy Syst.*, vol. 106, pp. 488 – 501, 2019.

[3] D. Chakravorty, B. Chaudhuri, and S. Y. R. Hui, "Rapid frequency response from smart loads in great britain power system," *IEEE Trans. Smart Grid*, vol. 8, no. 5, pp. 2160–2169, 2017.

[4] Y. Che, J. Yang, Y. Zhou, Y. Zhao, W. He, and J. Wu, "Demand response from the control of aggregated inverter air conditioners," *IEEE Access*, vol. 7, pp. 88 163–88 173, 2019.

[5] M. Malekpour, R. Azizipanah-Abarghooee, F. Teng, G. Strbac, and V. Terzija, "Fast Frequency Response From Smart Induction Motor Variable Speed Drives," *IEEE Trans. Power Syst.*, vol. 35, no. 2, pp. 997–1008, 2020.

[6] R. Azizipanah-Abarghooee and M. Malekpour, "Smart induction motor variable frequency drives for primary frequency regulation," *IEEE Trans. Energy Convers.*, vol. 35, no. 1, pp. 1–10, 2020.

[7] I. Ibrahim, C. O'Loughlin, and T. O'Donnell, "Virtual Inertia Control of Variable Speed Heat Pumps for the Provision of Frequency Support," *Energies*, vol. 13, no. 8, p. 1863, 2020.

[8] J. Vorwerk, U. Markovic, P. Aristidou, E. Vrettos, and G. Hug, "Modelling of variable-speed refrigeration for fast-frequency control in low-inertia systems," *IET Smart Grid*, vol. 3, no. 6, pp. 924–936, 2020.

[9] H. Huang and F. Li, "Sensitivity analysis of load-damping characteristic in power system frequency regulation," *IEEE Trans. Power Syst.*, vol. 28, no. 2, pp. 1324–1335, 2013.

[10] Y. Bao, Y. Yao, M. Hu, X. Chen, J. Zhang, and Q. Wang, "Demand response as a method for damping electromechanical oscillations of the power system," in *IECON*, Beijing, 2017, pp. 208–213.

[11] T. Weckesser and T. Van Cutsem, "Equivalent to represent inertial and primary frequency control effects of an external system," *IET Gener. Transm. Distrib.*, vol. 11, no. 14, pp. 3467–3474, 2017.

[12] A. Ortega and F. Milano, "Impact of frequency estimation for vsc-based devices with primary frequency control," in *ISGT-Europe*, Torino, 2017.

[13] ——, "Comparison of different pll implementations for frequency estimation and control," in *IEEE PES ICHQP*, Ljubljana, 2018.

[14] C. Roberts, J. D. Lara, R. Henriquez-Auba, B. K. Poolla, and D. S. Callaway, "Grid-coupled dynamic response of battery-driven voltage source converters," in *2020 IEEE SmartGridComm*, 2020, pp. 1–6.

[15] Y.-J. Kim, L. K. Norford, and J. L. Kirtley, "Modeling and Analysis of a Variable Speed Heat Pump for Frequency Regulation Through Direct Load Control," *IEEE Trans. Power Syst.*, vol. 30, no. 1, pp. 397–408, Jan. 2015.

[16] "Der Energieverbrauch der Privaten Haushalte 2000 – 2017: Auswertung nach Verwendungszwecken und Ursachen der Veränderungen," Prognos AG, Tech. Rep., 2018.

[17] "Schweizerische Elektrizitätsstatistik 2018," Bundesamt für Energie BFE, Tech. Rep., 2020.